LA-UR- 10-04396

Approved for public release; distribution is unlimited.

Title: A Comparison of HEVR Response in PBX 9501 and PBXN-9

Author(s): Laura Smilowitz, Bryan F. Henson, Jerry J. Romero, Blaine W Asay, Wendy McNeil, Mark Marr-Lyon and Paul Rightly, Gary P. Grim, Andy Saunders, Frank Merrill and Chris Morris,

Intended for: DOE Level Two Milestone Report

Los Alamos
NATIONAL LABORATORY
EST. 1943

Los Alamos National Laboratory, an affirmative action/equal opportunity employer, is operated by the Los Alamos National Security, LLC for the National Nuclear Security Administration of the U.S. Department of Energy under contract DE-AC52-06NA25396. By acceptance of this article, the publisher recognizes that the U.S. Government retains a nonexclusive, royalty-free license to publish or reproduce the published form of this contribution, or to allow others to do so, for U.S. Government purposes. Los Alamos National Laboratory requests that the publisher identify this article as work performed under the auspices of the U.S. Department of Energy. Los Alamos National Laboratory strongly supports academic freedom and a researcher's right to publish; as an institution, however, the Laboratory does not endorse the viewpoint of a publication or guarantee its technical correctness.

Form 836 (7/06)

A Comparison of HEVR Response in PBX 9501 and PBXN-9

Laura Smilowitz, Jerry J. Romero and Bryan F. Henson, *Chemistry Division*
Blaine W Asay, Wendy McNeil, Mark Marr-Lyon and Paul Rightly, *Weapons Experiments Division*
Gary P. Grim, Andy Saunders, Frank Merrill, Chris Morris, *Physics Division*
and the *pRad Collaboration*

Los Alamos National Laboratory
Los Alamos, NM

Abstract. We have completed a series of thermal explosion experiments on PBX 9501 and PBXN-9 and investigated their mechanism using proton radiography. In this paper we review the past five years of experiments utilizing radiographic techniques to study the mechanisms of internal burning in thermal explosions in these HMX based formulations. Experimental details of trigger timing and synchronization are given. Radiographic images collected using both protons and x-rays are discussed. Comparisons of experiments with varying size, case confinement, binder, and synchronization are presented. Analytical techniques for quantifying the data in the images are presented and a mechanism for post-ignition burn propagation in a thermal explosion is discussed. From these experiments, we have observed a mechanism for sub-sonic deflagration that involves both gas phase convective and solid phase conductive burning within the solid. The convective front velocity is directly measured from the radiographic images and consumes only a small fraction of the solid. It ignites exposed solid surface as it passes and begins the slower solid state conductive burning process. This mechanism is used to create a model to simulate the radiographic results and a comparison will be shown.

I. Introduction

Subsonic events in high explosives (HE) such as thermal explosion are inherently difficult to study.[1] Unlike a detonation, which can be started with very low timing jitter, thermal explosion timing is notoriously difficult to predict. The timing of a thermal explosion can span hours or days)[2, 3] with final ignition and post-ignition burn propagation occurring in tens of microseconds. This final switch in time scales occurs at a time controlled by the HE itself, which is subject to a nonlinear positive feedback whereby exothermic reactions increase local temperature and accelerate reaction rates. Further complicating studies of subsonic thermal explosion is the fact that post-ignition burn propagation occurs with velocities low enough that material and case conditions ahead of the reaction front can be communicated to the reaction front and influence it, another complication which is simplified in supersonic detonation. Experimentally, observing a thermal explosion with optical techniques such as fast framing cameras or spectroscopy are useful only until the case confinement is breached and light and smoke from the reaction obscure the diagnostics.

Despite the difficulties outlined, looking inside a thermal explosion is essential in order to understand the relevant phenomenology and to deconvolve the mechanisms which combine to control energy release. These questions ultimately

must be addressed in order to be able to predict reaction violence of an HE system subjected to an abnormal thermal environment.

Based on the need to observe the transition to ignition and post-ignition burn propagation in a thermal explosion, we have worked out several technical problems to allow radiographic imaging of thermal explosions. Radiography provides a measure of the evolution of density caused by material flow and decomposition leading up to ignition and then a measure of the rapid consumption of material during burn propagation subsequent to ignition. We have designed a small scale radial thermal explosion experiment, utilizing cylindrical symmetry, enabling research scale experiments.[4] We have applied thermal boundary conditions that drive ignition to a single central point, giving up traditional one dimensionality in exchange for the ability to predetermine the ignition location.[2, 4, 5] A model of pre-ignition thermal decomposition for HMX based formulations has been refined to the point where we can predict an ignition time with tens of seconds accuracy.[6] Triggering and synchronization techniques have been developed and will be discussed below.

We have fielded these thermal explosion experiments using two different types of radiography. We have collected multiple dynamic images of thermal explosion events using proton radiography at the Los Alamos National Laboratory Proton Radiography (pRad) facility,[7, 8] and we have collected multiple dynamic x-ray images at the Livermore National Laboratory Hydra Facility[9, 10]. These experiments have been performed using both the HMX (octahydro-1,3,5,7-tetranitro-1,3,5,7-tetrazocine) based formulations PBX 9501 (95 wt% HMX, 2.5 wt% nitroplasticizer, and 2.5 wt% estane, initial density 1.83 g/cc) and PBXN-9 (92 wt% HMX, 6 wt% DOA, and 2 wt% Hytemp 4454, initial density 1.74g/cc). In addition, two different aspect ratios have been investigated and two different case confinements used.

In this paper, we present radiographic images for thermal explosions in the configurations described above. We will compare burn propagation behavior between the two HMX based formulations as well as compare differences for a given formulation with different geometries and case confinement strengths. Analysis of the radiographic images obtained will be discussed. We will conclude by describing the understanding of ignition and subsequent sub-sonic burn propagation enabled by this data set.

II. Experiment

The radial thermal explosion experiment is designed to be a small scale, reproducible experiment with a controlled ignition location and a case made of low atomic number materials to be compatible with radiographic imaging.[4] For these experiments, a case of 1/8" thick aluminum is found to provide sufficient confinement at low enough areal density (the density integrated along the proton beam axis) to allow for reasonable radiographic imaging.[5, 8]

Two schematics of the experimental design used in these experiments are shown in Fig. 1. The assembly is composed of two half cylinders, each containing a cylindrical sample of HE encased in the radial cylindrical confinement and an endcap piece used for combining the halves together. The full cylinder is bound by a glue seal at the midplane and strengthened by bolts in the endcaps. All configurations discussed in this paper utilized 1/8" cylindrical wall thickness. Two different endcap thicknesses were used, 1/8" and 1/16", as will be indicated later. Our intial design was based on a ½" diameter, 2:1 aspect ratio cylinder, as shown in Fig. 1 top. Subsequently we showed that a larger diameter was required in order to observe burning for a longer period of time before the cylinder wall was reached by the convective front, leading to a 1:1 aspect ratio design, shown in Fig. 1 bottom.

Thermal boundary conditions were applied such that ignition occurred at the center of the cylinder radially, and displaced approximately 1 mm from the center plane axially.[4] We instrumented this midplane with internal thermocouples and fiber optics for the control and synchronization of triggering to be discussed below.[5, 11] A typical midplane instrumentation suite is shown in Fig. 2.

The typical temperature trajectory applied involved heating the cylindrical wall to 205 C over approximately one hour with hold points at 70 C

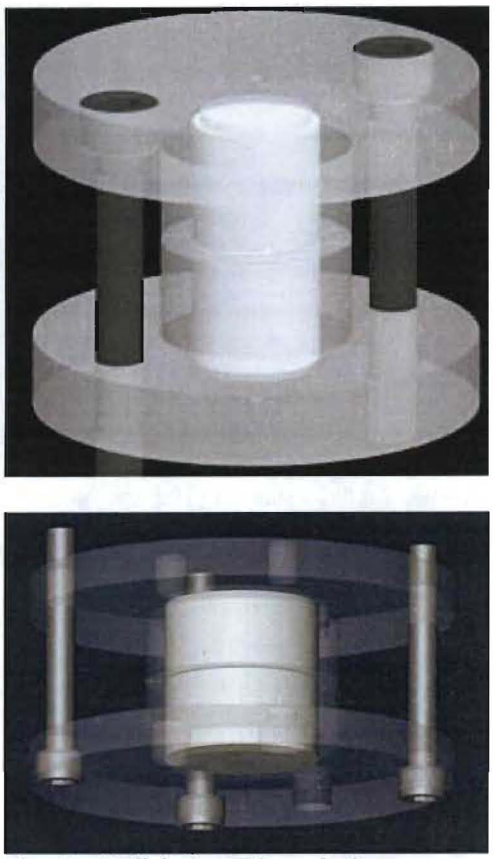

Fig. 1: Radial thermal explosion experiment schematics. White region is HE, grey is aluminum case, dark grey shows steel screws. Top: Initial 2:1 aspect ratio design. Bottom: 1:1 aspect ratio design.

and 178 C and heating rates of 5 C/min. This trajectory allows the HE to equilibrate and the final 205 C hold temperature allows the HE to self heat and develop a temperature gradient with the hottest point near the center of the cylinder.[5]

Thermal explosion experiments span time scales from the thousands of seconds laboratory time scale for the pre-ignition heat trajectory, to the acceleratory self heating and thermal runaway region lasting tens of seconds and creating internal heating rates of tens of degrees per minute, to the ignition regime and post-ignition burn propagation regime which take tens of microseconds for this scale of experiment. In order to capture observables spanning from hours to microseconds, we needed to develop triggering systems that

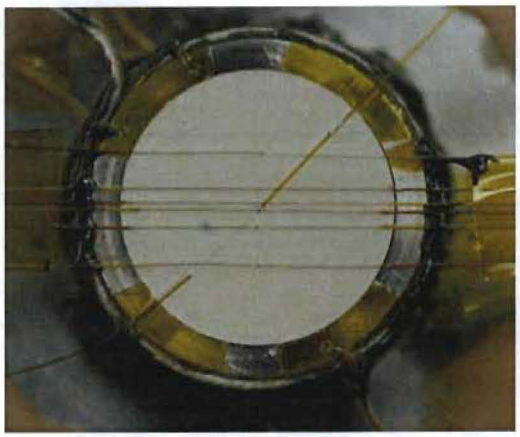

Fig. 2: Cylindrical midplane instrumentation looking at the internal midplane along the cylinder axis. Six 75 μm wire thermocouples and two larger, 200 μm optical fibers are shown.

could tell us when that switch in time scales was occurring. We have found that the internal thermocouples used to monitor self-heating can be used as a reliable trigger early enough in the breakout of ignition to trigger post-ignition diagnostics. A typical measurement made using a thermocouple placed close to the ignition volume is shown in Fig. 3.[2] A break-foil is used on the outside of the case as a timing fiducial for when the case comes apart, which we approximate as the

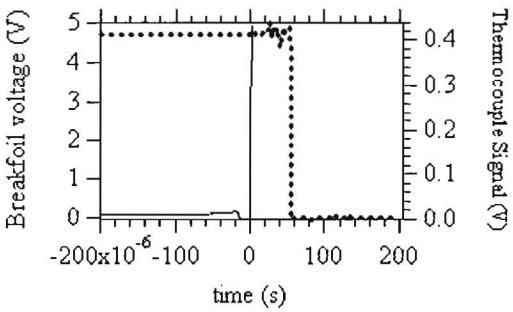

Fig. 3: Thermocouple trigger technique. Solid line is thermocouple direct voltage output. Dashed line is breakfoil signal.

end of useful data acquisition as the confinement has been fully lost by this point.

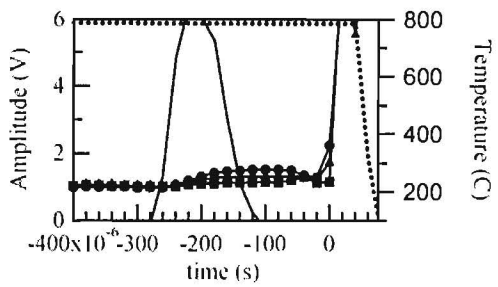

Fig. 4: Laser synchronization. Solid markers are temperature records for 3 thermocouples. Solid line is fiber to Silicon photodiode. Dashed line is breakfoil voltage.

In some cases, such as found at the pRad facility, being able to simply trigger external diagnostics when a thermal explosion event began was not enough. This facility is driven by an 800 MeV proton accelerator which delivers a 1 ms proton window every 50 ms, meaning that in order to capture a thermal explosion event, it needed to be synchronized to the pRad availability window. In order to do this, we developed a synchronization technique that would allow us to accelerate the thermal explosion sequence without drastically altering the natural event.[11] This technique involved using a fiber optic coupled to a free running Nd:YAG laser to provide a 150 μs temperature jump during the thermal runaway portion of the experiment. The laser pulse intensity measured using a second fiber optic and the temperature rise caused by the laser pulse are shown in Fig. 4. The internal thermocouples record both the temperature jump which accelerates ignition to within a few hundred microseconds and ignition itself, as a large voltage spike due to plasma. The ignition event triggers the oscilloscope at time zero and the external breakfoil records case failure approximately 30 μs later for the ½" diameter experiment and 60 μs for the 1" diameter. We have conducted a series of experiments varying the laser pulse energy and mapped out the ignition delay as a function of pulse energy. Details of the laser synchronization technique have been published elsewhere.[2, 11, 12]

Using these triggering and synchronization techniques, we have now run a series of experiments at both the pRad[8] and Hydra x-ray facilities.[10] In these experiments, we have compared effects of scaling shot size, formulation, case confinement, and synchronization.

III. Results: PBX 9501

A. The Response of PBX 9501

We now have 16 experiments that have been conducted at the pRad facility. The overall behavior we observe in the resulting images is that ignition is followed by crack propagation within ~ 10-20 μs at velocities from 300 to greater than 800 m/s depending upon endcap thickness, deformation and the state of axial tension resulting in the solid. The cracks continue to propagate and expand, but do not consume a large fraction of the HE. Subsequent to ignition, a wave is launched consistent with ~ 4% loss of HE density traveling at 200 to 300 m/s, independent of wall thickness or crack velocity. Following this for another ~50 μs is the slower loss of HE density as solid is consumed by conductive burning.

B. Radiography

A successful radiographic experiment requires synchronization of ignition with the proton window and material confinement both transmissive to proton illumination and of sufficient strength to enable pressurization and the observation of burning. Another variable is the confinement of gas phase products. The midplane seal is sufficient to allow pressurization throughout the heating of the sample, which is crucial to a reproducible pre-ignition boundary condition and thus reproducible time to ignition. The strength of the seal and bolt pattern are also such that the midplane opens along the cylinder axis at approximately the same time that internal thermocouple signals indicate the beginning of gas phase burning. This is also a crucial timing issue as the proton image contrast is dependent on removing high pressure gas phase products so that the resulting transmission change is dependent only on the evolution of the solid areal density. This results in a moving case edge which must be

considered when interpreting side view experiments, but does not effect the radial view, which does not show case motion until convection reaches the cylinder wall and elastic deformation begins. These effects will be noted as they are apparent in the images.

In the next two sections direct transmission images are shown, as they most clearly indicate the overall response during the experiment. This will be followed by more refined analysis, including image normalization, which will better reveal the fine resolution features, such as cracking and consumption, that are contained in the data.

1. Side View

Four frames from an experiment using a ½" diameter 2:1 aspect ratio sample are shown in Figure 5. Case confinement of 1/8" cylinder and endcap walls were used. The spatial resolution of these proton transmission images is approximately 100 microns. The grey scale in Fig. 5 uses white to represent high transmission (T=1) and black to represent low transmission (T=0). The endcaps are the black vertical bands and the vertical light line at the center is the midplane of the shot. The orientation of these images are rotated 90 degrees from figure 1 (top). The windings apparent in this experiment are due to the nichrome heater applied to the boundary in early experiments. A new design based on capton heaters was used in all subsequent experiments.

The times in each frame are relative to the internal thermocouple signal indication of gas phase burning. The opening of the midplane along the cylinder axis is apparent in the 26 and 40 μs frames. The escape of product gases from the midplane is also observed as the hemisphere emerging from the midplane, outside the cylinder edge, particularly in the 26 μs frame. Frames 54 and 61 μs show very high deformation later in the experiment.

Three frames from an experiment using a 1" diameter 1:1 aspect ratio sample are shown in Figure 6. Case confinement of 1/8" cylinder and endcap walls were used. The spatial resolution and transmission scale are the same as for Fig. 5. The orientation of these images are rotated 90 degrees from Fig. 1 (bottom). The general features of midplane opening, product gas escape and

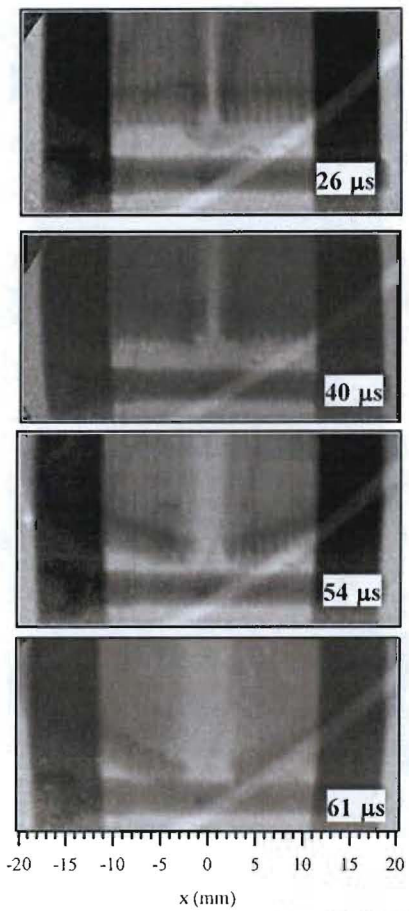

Figure 5: Proton transmission images of 1/2" diameter, 2:1 aspect ratio experiment imaged in side view. Half of the cylinder is shown. Case confinement of 1/8" cylinder and endcap walls were used. Frames times are relative to the rise of the internal thermocouple.

deformation are the same as for Fig. 5, however internal burning proceeds for much longer before a cylinder wall is reached by convective burning. This is a significant advantage during analysis and interpretation and is the reason that all subsequent experiments use this diameter and aspect ratio. The times in each frame are again relative to the internal thermocouple signal indication of gas phase burning.

Three frames from an experiment using a 1" diameter 1:1 aspect ratio sample are shown in Figure 7. Case confinement of 1/8" cylinder and 1/16" endcap walls were used. The spatial

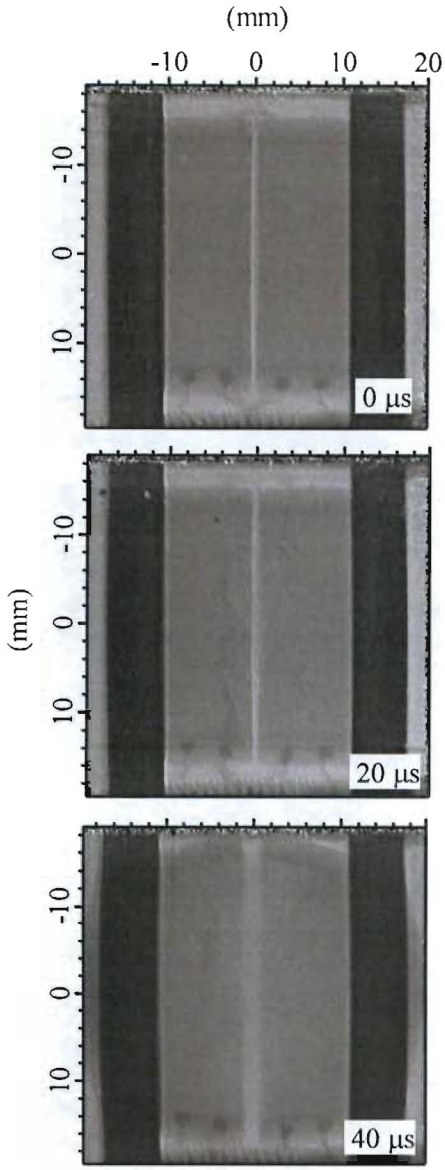

Fig. 6: Proton transmission images of 1" diameter, 1:1 aspect ratio experiment imaged in side view. Case confinement of 1/8" cylinder and endcap walls were used. Frames times are relative to the rise of the internal thermocouple.

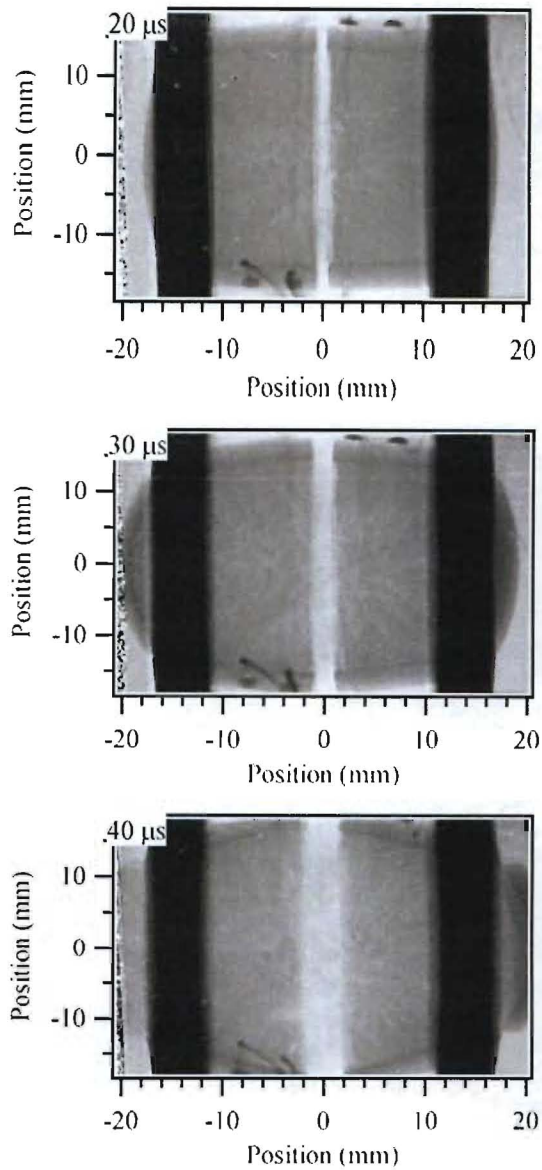

Fig. 7: Proton transmission images of 1" diameter, 1:1 aspect ratio experiment imaged in side view. Case confinement of 1/8" cylinder and 1/16" endcap walls were used. Frames times are relative to the rise of the internal thermocouple.

resolution and transmission scale are the same as for Fig. 5. The orientation of these images are rotated 90 degrees from Fig 1 (bottom).

The first frame shown is taken 20 μs after the thermocouple trigger. By this time, the endcaps are already visibly bowing, the center line has opened, and there is density loss and cracking visible in the HE. Frames were taken at 10 microsecond intervals. By the 40 μs frame, the endcaps have been punched out and the center aluminum plugs are flying outward. These plugs are typical of these shots and their velocities have been measured to be ~800 m/s. [10]

2. Radial View

Three frames from an experiment using a 1" diameter 1:1 aspect ratio sample are shown in Figure 8. Case confinement of 1/8" cylinder and endcap walls were used. The spatial resolution and transmission scale are the same as for Fig. 5. The primary observations from this view have been the crack patterns and radial wall motion observed in the images. The times in each frame are again relative to the internal thermocouple signal indication of gas phase burning.

3. X-ray Radiography

The proton transmission radiography requires laser synchronization in order to be able to capture dynamic images of thermal explosion during the less than 100% duty cycle of the proton accelerator. A sequence of four x-ray transmission images has been collected at the LLNL Hydra facility without requiring synchronization of the thermal explosion to the x-ray sources. This allowed verification that the laser synchronization technique did not significantly alter the outcome of the thermal explosion event. Details of the radial thermal explosion radiographed with four independent axis pulsed x-ray units was presented by Tringe at al the 14th International Symposium on Detonation. The behavior observed is similar to that observed with laser synchronized proton radiography. The velocity interpolated from the three radial views is approximate 300 m/s, in agreement with that measured in the laser synchronized pRad experiments. [10]

C. Image Analysis

We will discuss two forms of analysis with which to turn the radiographic images into

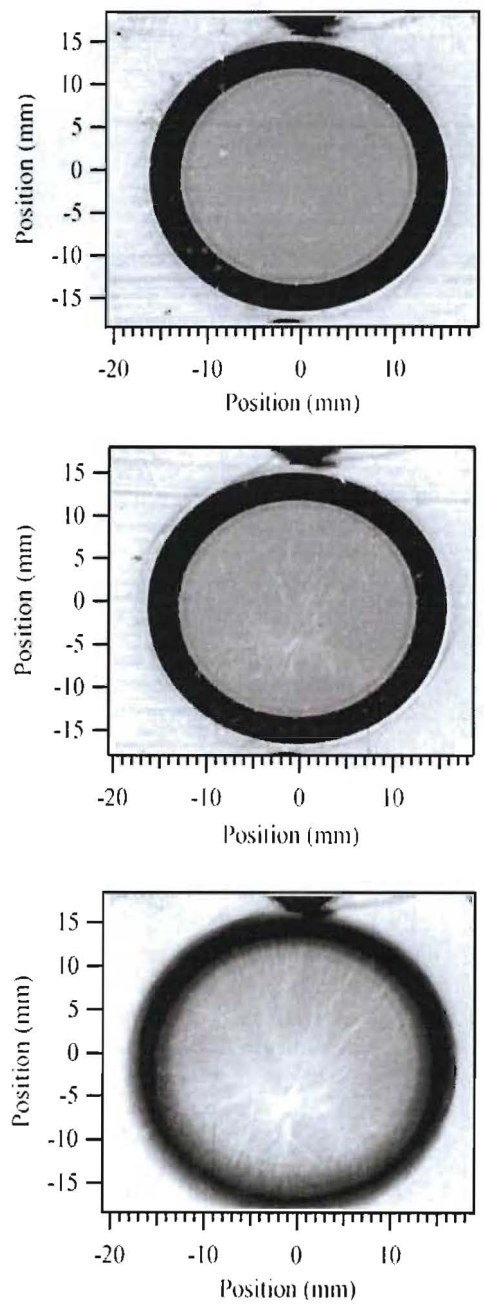

Fig. 8: Transmission images of 1" diameter, 1:1 aspect ratio experiment in radial view. Confinement of 1/8" cylinder and 1/16" endcaps were used. Frames were recorded at 20 μs intervals.

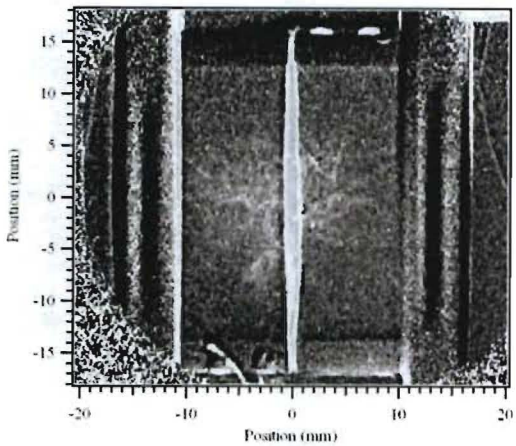

Fig. 9: Static normalization of the top image of Fig. 7.

digitized data. In the first we apply normalization techniques to elicit finely detailed changes in transmission during dynamic events by taking a ratio of the dynamic to a prior static image. In the second we perform various integrations of the transmission to obtain one dimensional line profiles of transmission that may be compared to calculated synthetic profiles.

1. Normalization

Fig. 9 shows the change in proton transmission by dividing the top image of Fig. 7 by a static image obtained a few minutes before the laser synchronization of thermal ignition. Taking the ratio of these two images allows enhancement of details of the change between these two images. It is similar to displaying the transmission image in logarithmic scale, or flattening the dynamic range of the image in order to bring out small changes in transmission. Presenting images as ratios of images taken before and during a thermal explosion event works well for small changes. The bright and dark bands in the image, particularly at the edge of the endcap and midplane are caused by motions of high contrast steps. A small displacement of a high contrast edge creates a large difference. What is clearly visible in this difference image is the density change in the HE which appears as white lines and a diffuse light region. The white lines look like cracks propagating to the endcap and the diffuse lightening would be caused by a loss of density during the burn propagation.

2. Integration of transmission profiles

Quantitative data is extracted from these images by drawing line profiles at various locations in the image and comparing these profiles at different image times. Fig. 10 shows an example of one frame with the region where the profile is collected and the actual wave generated. The peak at the midplane is where the case has begun to open and the transmission is approximately 0.9 where 1.0 represents the transmission through air. The fact that the transmission at the midplane is not 1.0 indicates high density gas and solid products are present. In fact, some of the products can be seen in the

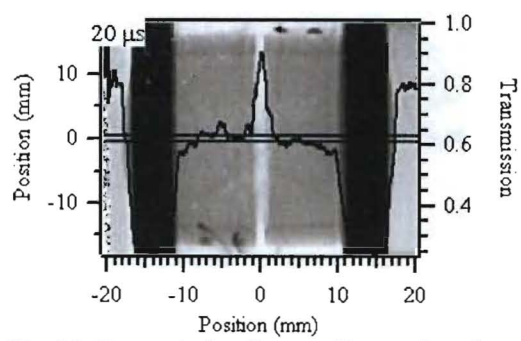

Fig. 10: Transmission line profile overlayed on image from frame taken 20 ms post ignition trigger. Horizontal grey lines show where the transmission profile was collected.

image. The transmission curve drops to about 0.25 in the aluminum endcap region. In the region between the midplane and endcaps, a plateau is observed with a slight gradient away from the midplane. This is due to the loss of HE density beginning at the midplane and then propagating towards the endcap. In subsequent frames, this density loss evolves. Another detail captured by the transmission profile is the fact that the transmission post-ignition is no longer flat, but has oscillations on it. These oscillations can be seen to correspond to spatial heterogeneities visible in the transmission images. They are not merely noise on a flat image, but represent a real phenomenon in the burn propagation; crack formation. The amplitude of the oscillation is a measure of the density loss in the crack.

By taking transmission wave profiles in the same spatial location from frames collected at different times relative to the thermocouple ignition trigger, a time sequence can be created. Fig. 11 shows the 8 frames taken between time 0 and time 80 microseconds (by which point the confinement was completely lost). Horizontal lines representing the proton transmission through air and through the initial density HE and aluminum case are included for comparison. The dashed line which is relatively flat at the initial HE/Al density is the line profile taken from an image prior to the onset of ignition. These profiles show the opening of the midplane, loss of HE density, and cracking in the HE (observable as oscillations in transmission). By plotting the approximate position of the leading edge of the transmission rise, a velocity can be extracted. We have performed such analysis on many experiments to date and determined typical axial convective velocities to be on the order of 200 to 300 m/s and radial velocities, measured with better precision, to be on the order of 160 to 180 m/s.

D. Preliminary Deflagration Model

Material in a thermal explosion is believed to be consumed by deflagration. Deflagration is the overall manner by which several sub-sonic processes combine to consume the material and

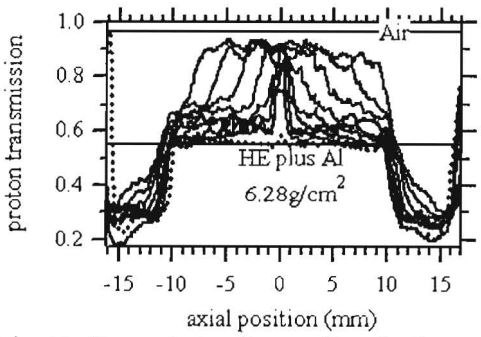

Fig. 11: Transmission line profiles for times from 0 to 80 μs after the ignition trigger. Horizontal lines show transmission for air and initial HE/Al. The dashed line is the profile from the pre-ignition static image.

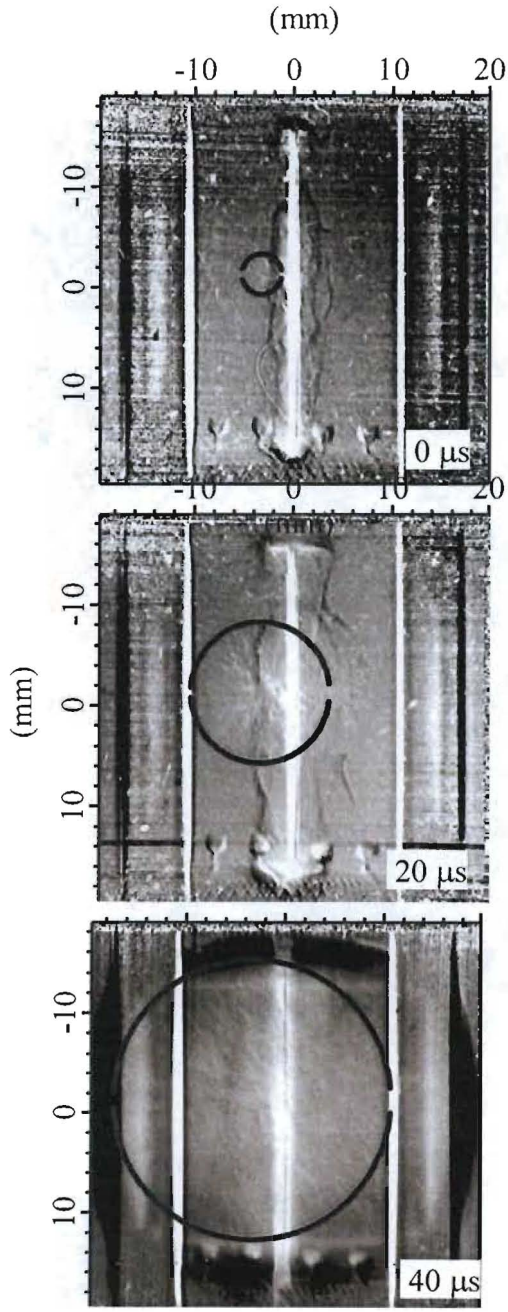

Figure 12: Normalized images from Fig. 6.

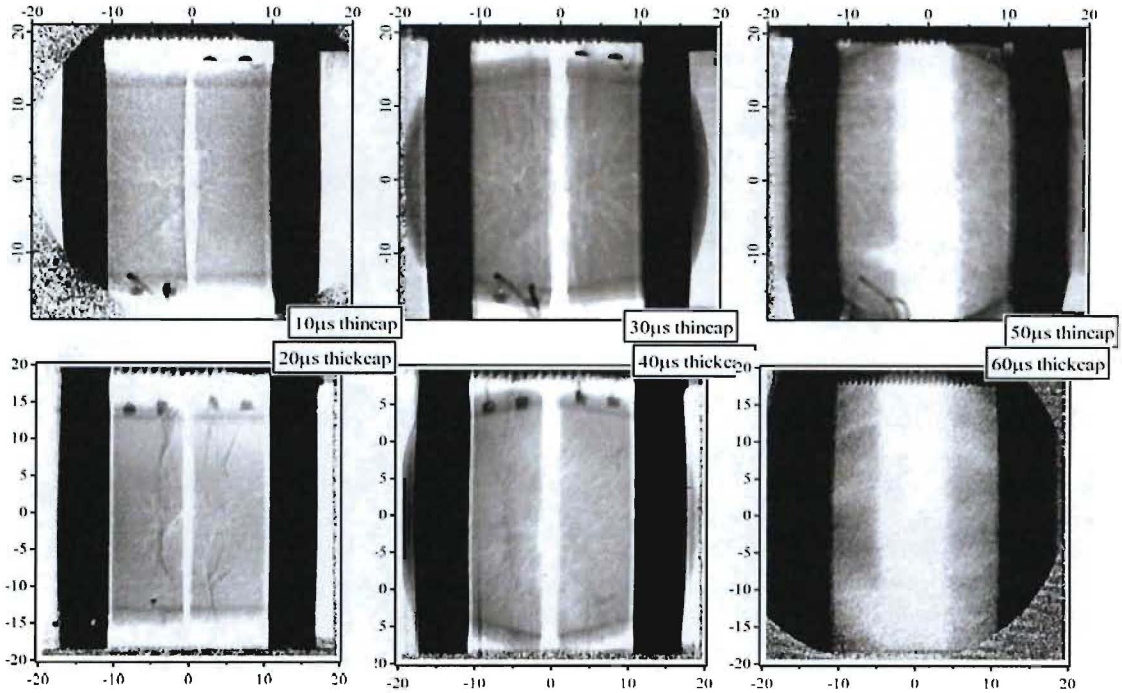

Fig. 13: Comparison of thin and thick endcap cases.

release energy by burning. Such processes include thermal damage or cracking, which expose material surface, conductive burning, the relatively slow (0.001 to 1 m/s) process by which solid is consumed and convective burning, where burning proceeds much faster (100 to 1000 m/s) through the gas phase by convection, and can ignite conductive burning on the exposed surface. The assertion that an explosion is driven by deflagration and adequately described by the component processes described above had remained an unproven hypothesis until this work, as there had been no means of directly observing these processes as they combine to consume solid and release energy. This has been a long standing problem throughout the Weapons complex. A principle product of this work is the verification that this hypothesis is essentially correct, and that with these new radiographic techniques we now have the tools to deconvolve the individual contribution of each mechanism to the overall deflagration behavior.

1. The role of cracking

Three normalized frames from the experiment shown in Figure 6 are again shown in Fig, 12. The black circles indicate the leading edge of the crack pattern, displaced by 1 mm from the center plane, and the radius as a function of frame time are used to calculate a velocity of 300 +/- 30 m/s for this 1/8" encap configuration. A significantly higher velocity is observed for the case configuration using a thinner endcap, as is shown in the normalized image in Fig. 9. This frame is the first dynamic frame obtained after the internal thermocouple trigger and the cracking pattern has already reached the endcap, a distance of 11 mm in less than 10 μs, indicating a lower bound velocity of 1100 m/s. The velocity of crack propagation is therefore a very sensitive function of the confinement, early deformation and the subsequent state of axial tension applied to the solid explosive early in the dynamic event. Comparative images from both experiments are shown in Fig. 13

2. Gaseous flame propagation by convection

A radially symmetric increase in proton transmission (decrease in density) can also be

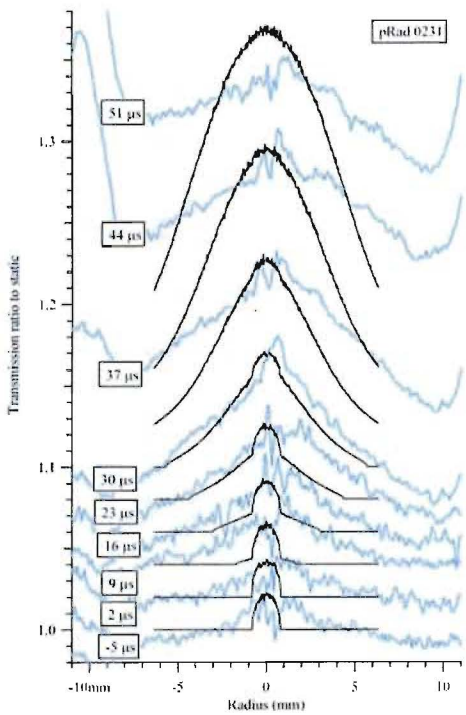

Fig. 14: Proton transmission data simulations. Black lines are simulations, grey lines are data, offset for clarity.

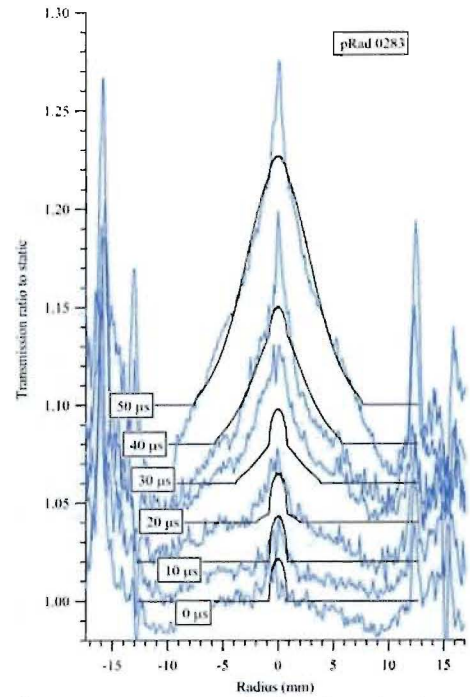

Fig. 15: Proton transmission data simulations. Black lines are simulations, grey lines are data, offset for clarity.

seen, superimposed on these crack patterns, from numerical analysis of the images. This is shown in Fig. 14 where the radial transmission intensity is plotted as a function of a ½" diameter radial view, starting 2 µs from ignition. These curves have been averaged azimuthally over 180°, such that each curve is a radial average over half of the cylinder, negative diameter representing one half and positive the other. Several bisecting planes were calculated, all with similar results. The symmetry is more evident in the negative diameter half of the cylinder using this bisecting plane but is nevertheless robust. The curves have also been normalized to one in the transmission through the unperturbed explosive.

At early times a relatively static volume of low density is observed in the center of the field. At approximately 16 µs the boundary of the radially symmetric feature begins to expand, and transmission within the feature increases. The boundaries of this feature reach the cylinder wall position 6.7 mm from the central ignition at approximately 37 µs. At this time, the increase in transmission becomes less radially distinct and by 51 µs appears relatively flat across the field. The side view images of Fig. 5 show intact cylinder wall position as late as 40 µs, indicating that the decrease in solid density in the radial view of Fig. 14 is not due to flow of solid material. The black solid lines are calculated from a model, to be described below, but as simple guides to the eye they enable a preliminary velocity of propagation of the transmission increase to be calculated, and indicate that model and data display some agreement until about 30 µs, with divergence at 37 µs consistent with the front reaching the radial confinement.

This same azimuthally averaged, radial integration is shown for a 1" diameter experiment in Fig. 15. The overall behavior is similar, however it is clear that the increased diameter provides an accurate measurement of the deflagration out to 50 µs, nearly doubling the time

to observe the transmission increase within the solid explosive.

Our interpretation of this radially symmetric structure is the propagation of a convective burn front by gas phase permeation through the material, followed by the loss of solid by conductive burning. This suggests a mechanism based on one dimensional convective[13] and conductive[14] burning in HMX. In this mechanism of internal, radially divergent burning, a propagating convective front ignites the solid, which is then consumed by a conductive burn.

3. Conductive burning and solid consumption

Conductive burning is the actual consumption of solid by burning. The rate of regression of the burning surface is determined by the surface temperature, which is a function of the distance of the flame from the surface. This distance is itself a function of pressure, therefore the rate of regression is an indirect function of the pressure. One dimensional linear regression as a function of pressure is relatively well understood and measured in a number of energetic materials, including HMX.

What we are concerned with here in internal burning is the rate by which linear regression, superimposed on a complex solid morphology, consumes the solid and releases energy. This is of course a very complex function of the solid morphology, as illustrated in Figs. 16 and 17. In the bottom panel of Fig. 16 the trimodal, post pressing particle distribution measured for PBX 9501 is shown in grey, along with the integration of this distribution in the top panel.[15] A simulated distribution to be discussed later, based on a model of thermal damage, is shown as the black line in both panels.

The post pressing distribution is integrated using two models of consumption and the resulting progress of consumption as a function of time are shown in Fig. 17. In Fig. 17a a surface regression model is assumed, where the distribution of particles is ignited on the surface and regresses toward the center. In Fig. 17b an inverse regression is assumed, where particles are ignited from the center and regression consumes the particle in the opposite direction. Both models are simplifications of more complex aggregate processes where burning occurs through much

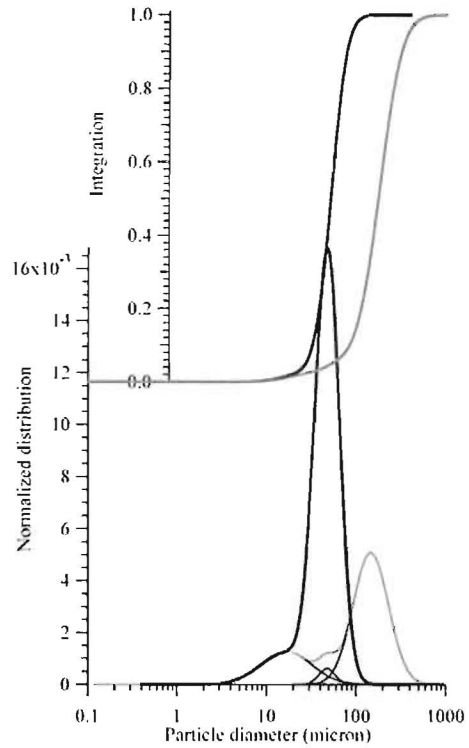

Fig. 16: Bottom: Post pressing particle distribution in PBX 9501 (grey) and a simulated distribution based on a damage model. Top: Integrations of the two distributions.

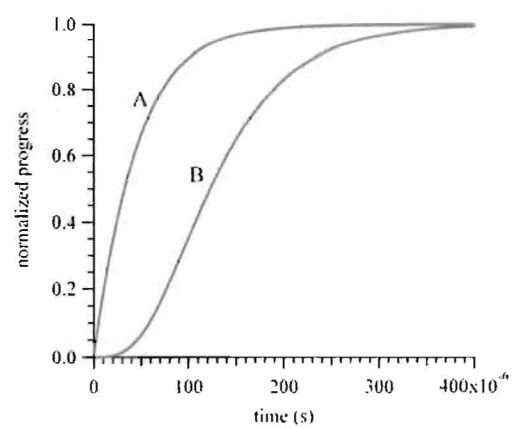

Fig. 17: Progress functions describing the consumption of solid as a function of time assuming a regression rate of 1 m/s.

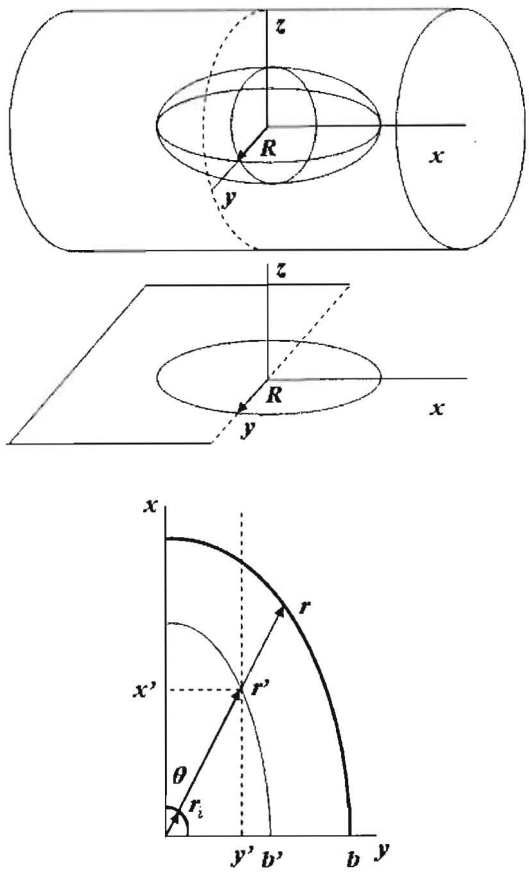

Fig. 18. Three projections of the coordinate axis used to describe the emanation of the convective burn front from the center of the cylinder to the outside walls.

more complex porous and cracked features, but are never the less very useful simplifications. In the next section we describe how we determine how to combine and constrain these components of the deflagration as they combine to release energy in these experiments on PBX 9501.

4. Model

We present here a preliminary, simplified composite model of the deflagration and energy release in the first experiments on PBX 9501.[8, 16]

We first make the assumption that the important characteristics of the morphology in this problem are created by processes at work during the heating of the solid prior to ignition, rather than the extensive cracking that we observe dynamically post ignition. We make this determination based primarily on two observations. Firstly the velocity of the cracking patterns observed differ by nearly a factor of three as a function of axial confinement, as shown in Fig. 13, yet using analysis of convective velocities such as described and shown in Fig. 10, the convective velocities are the same to within the measured uncertainties in these two configurations. Secondly, the β–δ phase transition in HMX is a likely candidate for pre-ignition thermal damage, and could be responsible for the independence of the convective rates on dynamic crack propagation. In addition, we will show below that a possible model of morphology and conductive burning is consistent with a particle size component in the PBX 9501 distribution that may represent a damage mode, i.e. a component whose contribution to the total increases with damage, in this case pressing. So, while much work remains to further validate these hypotheses we proceed to describe a bulk burning model of these experiments, independent of the observed crack formation and propagation.

We have developed a Monte Carlo (MC) simulation of the combined convective ignition/conductive consumption model. A schematic of the cylindrical solid explosive piece, including an ellipsoidal convective front emanating from the origin of a Cartesian coordinate system centered in the midplane of the cylinder, is shown at the top of Fig. 18. The model assumes an axis of revolution about the cylinder axis and a plane of symmetry bisecting the cylinder at the midplane. The resulting two dimensional projection is shown in the middle of Fig. 18. The projection is labeled in the bottom of Fig. 18 as an ellipse with semimajor axis a along x and semiminor axis b along y. Also labeled are rays from the origin denoting the boundary of the initial ignition volume, r_i, and two contours representing the progress of the convective burn front at r' and r.

The semimajor axes represent the furthest extent of the convective burn at a given time t since ignition, projected along the two orthogonal axis of the cylinder. Viewed down the cylinder axis the semiminor axis b can be directly measured

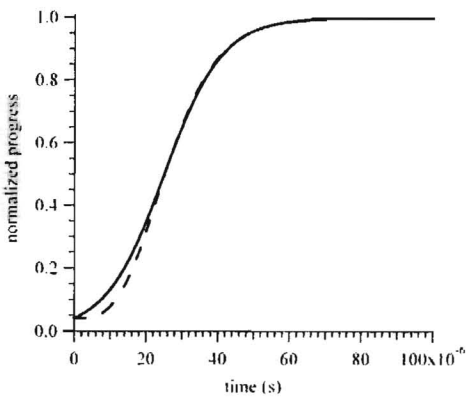

Fig. 19: Progress functions describing both the fit progress (solid) and the consumption of solid as a function of time assuming a regression rate of 1 m/s and the thermally damaged particle distribution (dashed).

from the radiograph as the leading edge of the propagating transmission increase. Viewed from the side (orthogonal to the cylinder axis) the semimajor axis a can be similarly measured. Dynamic images of several frames enable the velocity of propagation along either projections to be measured, *i.e.* $v_i = i/t$ where v is the velocity and the index i is either a or b.

The consumption of material as a function of time behind the convective front is calculated as follows. At a time t the MC routine samples points along the 12.7 mm line of site through one half of the cylinder at points along the diameter. Points (x',y') for which

$$\sqrt{r_i^2 - y'^2} < x' < \sqrt{a^2(1-(y'/b))^2} \qquad (1)$$

lie outside the location of the convective front at that time and are assigned a progress variable of zero. Points for which $y' < r_i$ and

$$x' < \sqrt{r_i^2 - y'^2} \qquad (2)$$

lie within a volume about the center assumed to be consumed by ignition and are assigned a progress variable of 1. For points between these limits the time is calculated since the passage of the convective front, this being the time during which consumption by conductive burning has proceeded. For such a point on the diameter, y', and a point along the cylinder length, x', in Fig. 18 this time is given by

$$\Delta t = \frac{b - b'}{v_b} \qquad (3)$$

where b and b' are the semiminor axes of the current position of the convective burn front at $r(t)$ and a previous position $r'(t\text{-}\Delta t)$. Let $b = R$ and

$$b' = r'\sqrt{(1-(\varepsilon\cos(\theta))^2} \qquad (4)$$

where

$$r' = \sqrt{(x'^2 + y'^2)} \qquad (5)$$

and

$$\theta = \arctan(y/x) \qquad (6)$$

Substituting Eqs. (4-6) into Eq.(3) yields

$$\Delta t = \frac{R - \sqrt{(x'^2+y'^2)(1-(\varepsilon\cos(\arctan(y'/x'))^2}}{v_b} \qquad (7)$$

where Δt is the time since passage of the convective front, v_b the convective front velocity in the radial direction and R is the current radius of the convective front ($R = v_b t$, where t is the frametime for each of the simulated curves in Figs. 14 and 15) To allow for the possibility of a faster convective rate along the axial direction, ε is an

Ignition volume	
r_i	0.8 mm
Convective velocities	
v_a	280 m/s
v_b	190 m/s
Consumption parameters, Eq. (8)	
thalf	25 μs
rate	7 μs

Table 1: Parameters of the transmission simulation for Figs. 14 and 15.

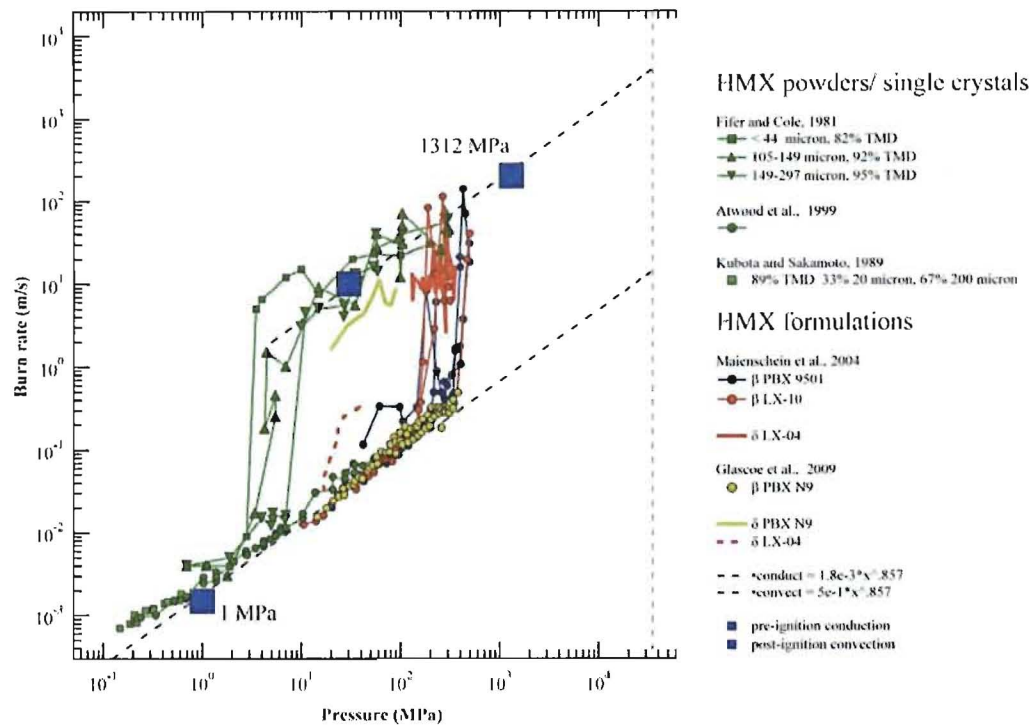

Figure 20: Burn rate as a function of pressure for HMX.

elliptical eccentricity equal to $\sqrt{(1-(\alpha)^2)}$, where α is the ratio of the axial over the radial velocities. The extent of consumption is then calculated from a sigmoidal function, based on this time, as

$$p(\Delta t) = \frac{1}{1+\exp(-(\Delta t - thalf)/rate)} \qquad (8)$$

where p is a progress variable spanning 0 to 1 over approximately 20 μs and proportional to density. The sum of values at each MC step, 0 for material ahead of convection, 0 to 1 in the volume, and 1 for completely consumed, is integrated and normalized, yielding a density normalized to 1 at full density. The calculation of density is then converted to transmission and normalized for comparison to Figs. 14 and 15.

The parameters of the simulations are shown in Table 1. The comparison of simulated transmission and two sets of experimental profiles viewed in the radial direction are shown as the solid lines in Figs. 14 and 15. The only difference in the two calculations is the aspect ratio for the line integrations, which reflects the two different geometries.

As described above, the convective velocities constrain the progress of the transmission increase across the radius of the image and the subsequent consumption determines the shape and magnitude of the transmission increase as a function of time. The parameters of the function describing consumption, Eq. (8) were fit to the data of Figs. 14 and 15, and generate the progress function shown as the bold black line in Fig. 19. Although this progress function results from a fit to the transmission data, and a unique attribution of a consumption mechanism from such a fit is not possible, this function does correspond closely to a progress function which does follow from a particular morphology model.

Both convective and conductive burn rates are functions of the gas phase pressure above the burning surface. A compilation of measurements of burn rate as a function of pressure from several groups and for several formulations of HMX are shown in Fig. 20. Data for HMX pressed powders

are shown in both confined and unconfined experiments (green squares and triangles)[17] and linear measurements of HMX powders (green circles and squares).[18, 19] Linear regression measurements of laminar burning to deconsolidation are shown for plastic bonded formulations of HMX, PBX 9501 (blue),[14] LX-10 (red),[14] and PBX N-9 (yellow).[20] Data are also shown from linear regression experiments on thermally damaged HMX formulations LX-04 (dashed red),[14] PBX N-9 (yellow) [20] and LX-10 (solid red).[14]

The lower, linear grouping of data are measurements of regression during conductive burning of the solid. The upper grouping, beginning with transitional progress from the lower line to the upper at around 2-10 MPa, are measurements of convective rates. In these subsonic experiments, while gradients in the gas phase pressure surely exist, we adopt a first approximation of quasistatic equilibrium, such that both convective and conductive burn rates must correspond to a single system pressure. We further make the key assumption in these simulations and indeed our overall interpretation of these results, that the dependence of burn rate on pressure measured for HMX in Fig. 20 applies unmodified to the internal burning observed in these experiments. This is an assumption here, but in a larger sense the validation or negation of this hypothesis is the primary motivation of this work.

This assumption allows us to use the observed velocity of convection, 280 m/s for the axial velocity, and infer a pressure from the data of Fig. 20, ~ 1.3 GPa. We then evoke the assumption of equilibrium and note that the conductive velocity at ~ 1.3 GPa is ~1 m/s. Note that this was the velocity of regression used in the calculation of progress functions from the post pressing PBX 9501 particle distribution shown in Fig. 17. If we perform the same integration on the damage mode distribution shown in Fig. 16, and assume an inverse regression model, we obtain the progress function plotted as the dashed line in Fig. 19, in remarkable agreement with the progress function fit to the transmission data. While this is certainly not a necessary attribution, it is a compelling result.

The results of the simulations suggest a number of preliminary conclusions. As we are able to simulate two different experimental configurations with the same morphology model they lend support to the assertion that the important characteristics in the morphology for burning are introduced prior to ignition (and likely during the phase transition). They further illustrate the observables and calculated products from the image data, and how the component mechanisms of burning in the internal deflagration may be isolated and measured. And finally they tend to support the hypothesis that the functional dependence of burn rate on pressure is conserved in the internal burning environment.

IV. Results: PBXN-9

A. The Response of PBXN-9

Finally, we describe the results of proton radiographic experiments done on the navy HMX formulation PBXN-9 specifically to directly compare dynamic response from two different HMX formulations. These experiments were conducted and imaged radiographically in a configuration nominally identical to the PBX 9501 experiments of Fig. 6, conducted in the 1/8" side by 1/8" endcap configuration. Nominally identical thermal boundary conditions and laser synchronization techniques were also applied.

Despite both formulations having high HMX content by weight (95% HMX in PBX 9501, 92% HMX by weight in PBXN-9), the PBXN-9 dynamic response is dramatically different than that observed from PBX 9501.[21] This difference is very reproducible and has been observed in a number of experiments, including those presented here that were imaged by radiography.

a

b

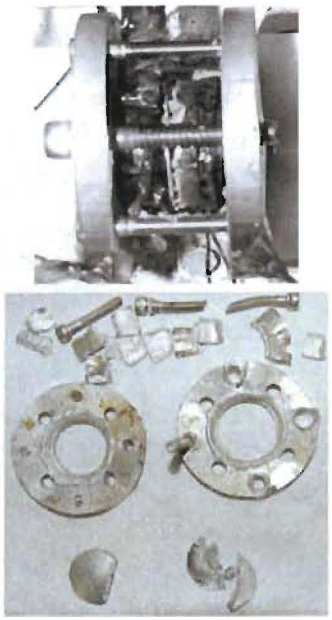

Fig. 21: a) Postmortem photos of PBXN-9 thermal explosion. b) Postmortem of 9501

The pre-ignition behavior of PBXN-9 is similar to that of PBX 9501. The beta to delta phase transition is observed to persist for approximately 10 minutes at the 178 °C boundary temperature. Internal temperatures exhibit the exothermic decomposition at the 205 °C boundary temperature as seen for PBX 9501. The time to ignition for PBXN-9 is longer than the time to ignition with the same boundary temperature for PBX 9501. Ignition time for PBXN-9 is 39 minutes compared to 23 minutes for PBX 9501 at the boundary temperature of 205 °C.

The post-ignition behaviors of the two formulations show significant differences. The first evidence for this difference is the postmortem analysis of the residue. The remainder from PBXN-9 and PBX 9501 radial experiments with the same applied temperature boundaries are shown in Fig. 21. The PBX 9501 is completely consumed, the aluminum sidewalls are fragmented, and the end caps have discs punched out where the convective wave impacted the wall. The PBX 9501 is seen in proton radiography images to balloon out from a cylinder to a sphere during the approximately hundred microseconds of the thermal explosion event, as observed in Figs. 5-7.

In contrast, the PBXN-9 experiments remain largely intact after ignition and burning. Approximately 50% of the HE remains after the thermal explosion and the aluminum case is distorted, but not fragmented. Typically the endcaps are not punched out and are only slightly deformed from flat.

B. Radiography

The proton radiography of the PBXN-9 thermal explosion event allows one to observe the post-ignition burn propagation and to measure the density loss caused by the HE burning. One frame of the density evolution movie taken during the thermal explosion event is shown in Fig. 22. This frame was collected 320 microseconds after the onset of the central ignition. Fig 22b shows the density profile at different distances from the midplane of the shot at this particular frame time. The maximimum density loss occurs at the midplane with a decrease of 60% of the initial HE

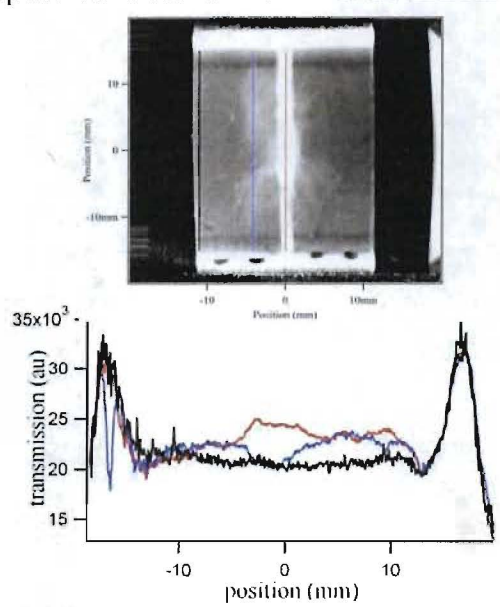

Fig. 22: Proton radiograph taken of a PBXN-9 experiment 320 microseconds into thermal explosion. Bottom data are vertical line profiles of image at various axial locations as marked in (a).

density[2]. Further from the midplane, density loss is approximately 40%, and furthest from the midplane, near the endcaps, there is little density loss.

Six frames from an experiment using a 1" diameter 1:1 aspect ratio sample are shown in Figure 23. Case confinement of 1/8" cylinder and endcap walls were used. The spatial resolution and transmission scale are the same as for Fig. 6, a directly comparable PBX 9501 experiment. The orientation of these images are rotated 90 degrees from figure 1 (bottom). The general features of this experiment are much slower than those of the PBX 9501 experiment shown in Fig. 6, with no wall deformation observed at 320 μs after ignition. Another significant difference is the pattern of cracking. While cracking is extensive and very finely divided in PBX 9501, reminiscent of the shattering of a brittle solid, the crack patterns here more resemble a side view integration of the classic conical failure surfaces of a homogenous, compliant solid under tension.

There are 23 proton radiographs collected at 16 μs time intervals during the thermal explosion experiment shown in Fig. 23. By taking a line profile across the midline of the images and overlaying the profiles for all images, a burn velocity can be extracted by tracking the edge position as a function of time. Fig 24 shows these overlaying line profiles. The very high transmission feature at the midplane of the cylinder is the opening of the wall, but following the smaller transmission increase, particularly to the negative half cylinger, allows the tracking of convection, as in the PBX 9501 experiments. The burn velocity extracted from them shown in Fig. 25 is 10 m/s.

C. Modeling

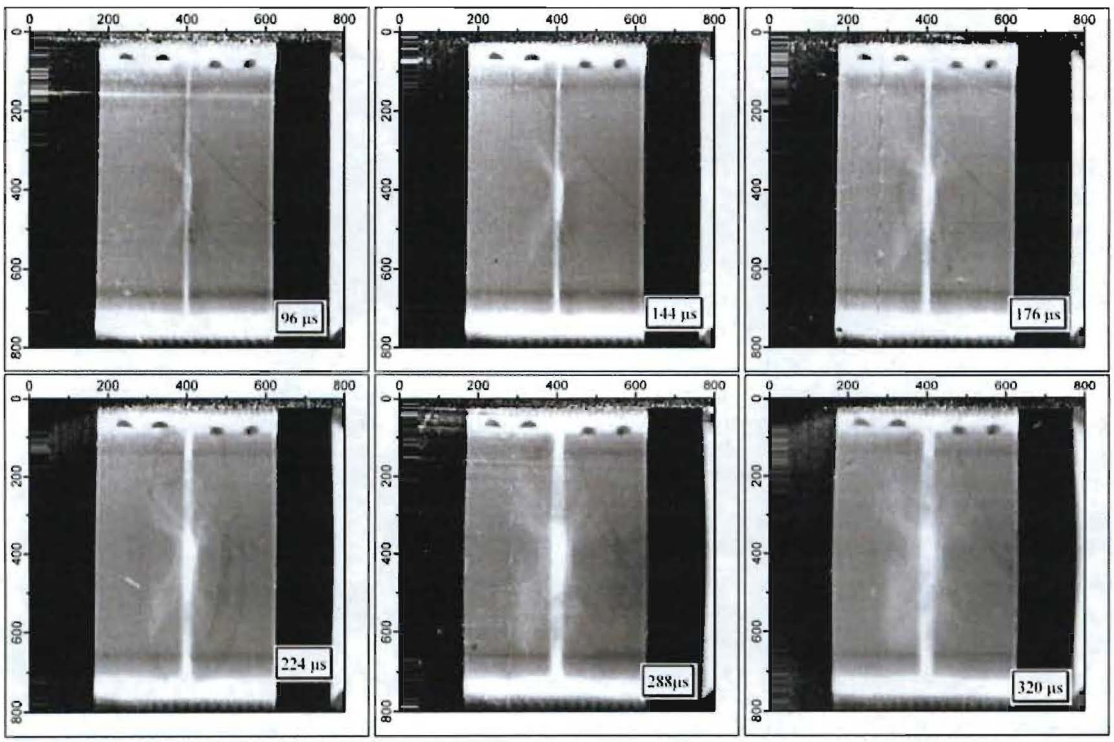

Fig 23. Proton transmission images of 1" diameter, 1:1 aspect ratio PBXN-9 experiment imaged in side view. Case confinement of 1/8" cylinder and endcap walls were used. Frames times are relative to the rise of the internal thermocouple.

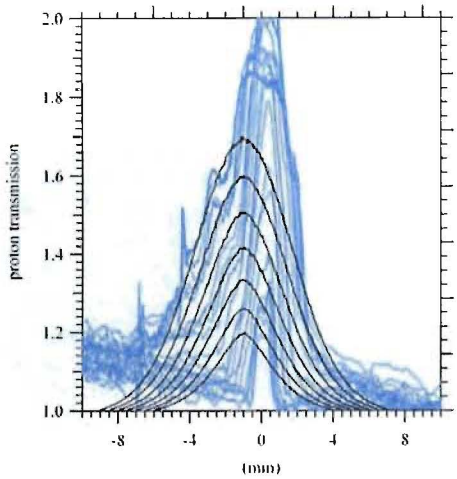

Fig. 24: Horizontal line profiles from proton radiographs of PBXN-9 thermal explosion taken from time 0 to time 384 microseconds into the event.

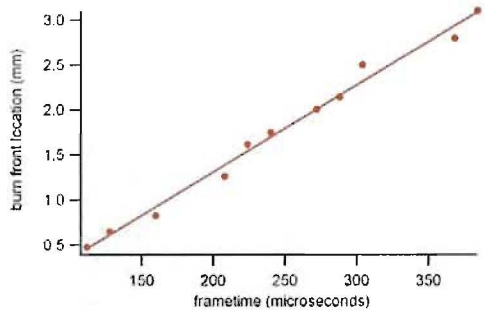

Fig. 25: Velocity data extracted from profiles in Fig. 24.

We have performed preliminary simulations of the profiles of Fig. 24. These calculations were done as for Section III.D.4. From the edge measurements of Fig. 25 we use a convective velocity of ~ 15 m/s and an inferred pressure from Fig. 20 of 30 MPa. This indicates a conductive velocity of ~0.1 m/s. We generate a progress function by once again integrating an inverse consumption model of the damage mode particle distribution, as we did for the simulations of PBX 9501, this time with a regressive velocity of 0.1 m/s. The resulting progress function is shown in Fig. 26. The final simulations are shown as the black lines in Fig. 24, with parameters listed in Table 2. The simulation was integrated in the side view configuration, with ignition displaced 1mm to the negative cylinder half. Visual interpretation is made somewhat difficult by the increased transmission at the midplane in this view due to case opening, but the simulation captures the overall structure of the transmission increase due to HE consumption.

Ignition volume	
r_i	0.0 mm
Convective velocities	
v_a	25 m/s
v_b	15 m/s
Consumption parameters, Eq. (8)	
thalf	200 μs
rate	55 μs

Table 2: Parameters of the transmission simulation for Fig. 24.

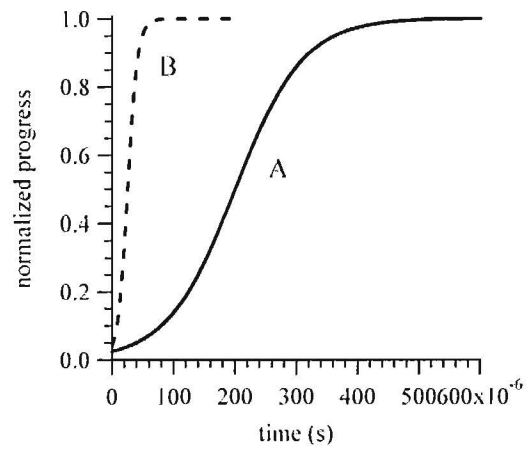

Fig. 26: A) Progress function describing the consumption of solid as a function of time assuming a regression rate of 0.1 m/s. B) Progress function for the PBX 9501 simulations in Figs. 14 and 15 for comparison.

V. Comparison of PBX 9501 and PBXN-9 Response

The proton radiographs for thermal explosions of PBX 9501 and PBXN-9 are directly compared

using three representative frames in Fig. 27.[4, 21, 22] The top 3 images are taken 20 microseconds apart during a PBX 9501 thermal explosion event. The first frame is early in the event and shows cracking from the midplane and product gas escaping from the midplane opening. The 2nd frame taken 20 microseconds later shows the aluminum case has been distorted from a cylinder to more spherical. By the 3rd frame 40 microseconds after the first, the midplane has opened, the case has been severely distorted and the aluminum has begun to fragment. In comparison, the bottom 3 images are taken 64 microseconds apart. In the first frame, density loss and cracking from the midplane are observed. This pattern expands by the 2nd frame, 64 microseconds later, but has not yet reached the endcaps nor significantly distorted the aluminum cylinder. The final frame shows continued density loss and growth of the pattern, without any fragmenting of the aluminum cylinder and only slight bowing of the endcaps. The postmortem analysis of this shot shows that the state of the radial case does not change significantly after the final proton radiograph collected during the thermal explosion event. Fig 21 above shows what is left of the case after the shot has cooled back down to room temperature. There is damage evident at the midplane, and evidence of hot gases having escaped. More than 50% of the PBXN-9 remains in the case and there is unconsumed HE found outside the case as well. Some wall and endcap bowing is seen.

The overall response of PBXN-9 in a thermal explosion is lower reaction rate, lower total energy, and lower reaction violence than for PBX 9501 under the same conditions. The post-ignition burn velocity for PBXN-9 is 20 times lower than PBX 9501, the total material consumed is approximately half, and there is significantly less damage to the confining case for PBXN-9 than PBX 9501. These observations are all consistent with a lower pressure impulse and lower sustained

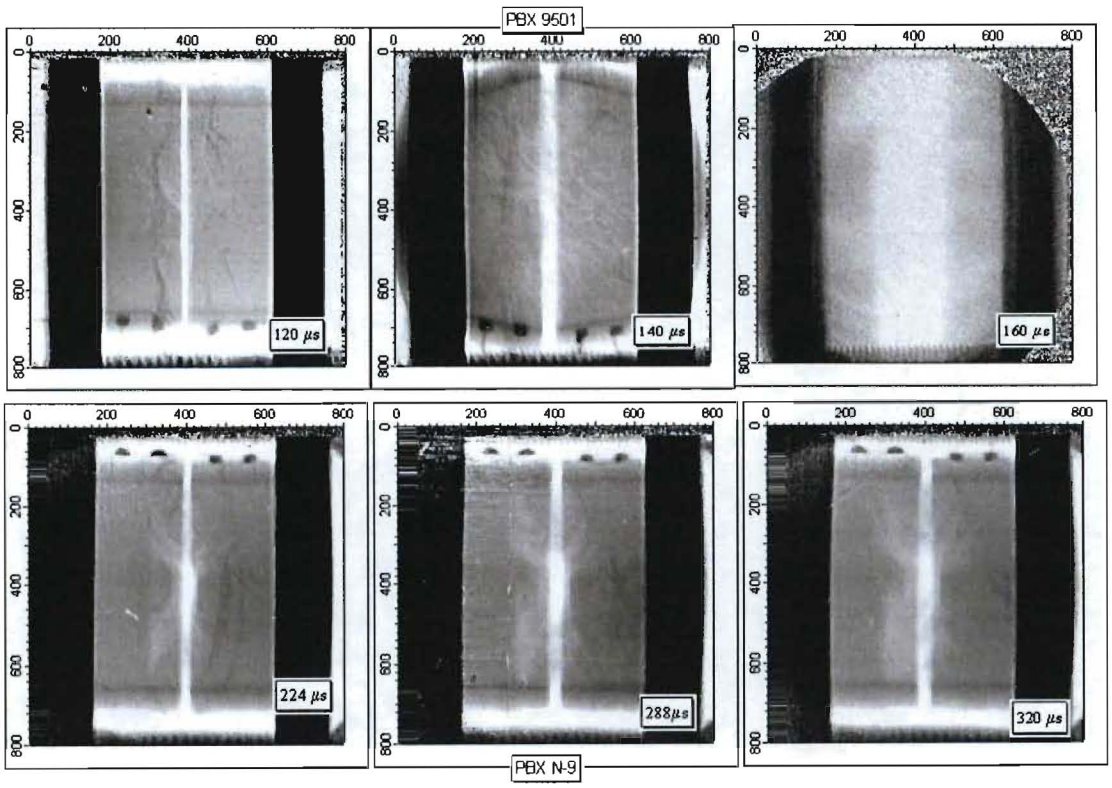

Fig 27. A direct comparison of PBX 9501 and PBXN-9 response

pressure for the PBXN-9 thermal explosions.

The deformation of the aluminum case can be analyzed as a strain record of the thermal explosion. The spatial resolution of the pRad images is approximately 100 microns. The side walls for the PBXN-9 experiment does not move during the thermal explosion event, implying a strain upper bound of L+100 microns/ L, which equates to 50 MPa for the aluminum alloy from which the case was made.

Fig. 20 shows a compendium of data for burn velocity verses pressure in HMX based formulations. The data falls on two different lines- a slower conductive burn line and a several order of magnitude faster convective burn line. The two large open squares on this graph are the velocity observed for the PBX 9501 thermal explosion. The pressure that would drive this burn velocity in a 1-dimensional linear burn would be approximately 1 GPa. The lower velocity point is the 10 m/s burn rate observed in PBXN-9 and is consistent with a convectively driven burn with pressure ~ 20 MPa. This pressure is consistent with the upper bound inferred by the optical strain limit of 50 MPa.

VI. Conclusions

In this work we have demonstrated the ability to radiograph thermal explosions, both using laser synchronized experiments at the LANL proton radiography facility, and using auto-ignition experiments at the LLNL Hydra multi-head x-ray facility. The utility of radiographic observables is their ability to provide a view inside a thermal explosion. From these experiments, we have been able to understand the mechanism of a thermal explosion and have put together a model capturing both the gas phase convective and solid state conductive components of a deflagration wave. Several parameters have been investigated including scaling the size of the HE and changing case confinement strength. In addition, we compare two different binder formulations having very different thermal responses and study the origin of that difference via radiography. We are currently beginning a series of longer aspect ratio shots with the potential to undergo a deflagration to detonation transition.

Acknowledgements

This research was conducted at Los Alamos National Laboratory with the support of the Joint Munitions Program and Science Campaign Two, for the Department of Defense and the Department of Energy, National Nuclear Security Administration.

References

1. B. W. Asay, in *Shock Wave Science and Technology Reference Library*, edited by Y. Hori (Springer-Verlag, Berlin, 2009), Vol. 5, p. 617.
2. L. Smilowitz, B. F. Henson, M. M. Sandstrom, et al., AIP Conference Proceedings **845**, 1211 (2006).
3. J. J. Yoh, M. A. McClelland, J. L. Maienschein, et al., Journal of Applied Physics **100**, 073515 (2006).
4. L. Smilowitz, B. F. Henson, M. M. Sandstrom, et al., Thirteenth Symposium (International) on Detonation, 1026 (2006).
5. L. Smilowitz, B. F. Henson, J. J. Romero, et al., AIP Conference Proceedings **955**, 1139 (2007).
6. B. F. Henson, L. Smilowitz, J. J. Romero, et al., in *Shock Compression of Condensed Matter*, edited by W. T. B. M.L. Elert, M.D. Furnish, W.W. Anderson, and W.G. Proud (AIP, Nashville, TN, 2009), Vol. 1, p. 257.
7. C. T. Mottershead and J. D. Zumbro, Proceedings of the IEEE Particle Accelerator Conference **2**, 1397 (1998).
8. L. Smilowitz, B. F. Henson, J. J. Romero, et al., Physical Review Letters **100**, 228301 (2008).
9. P. C. Souers, H. G. Andreski, J. Batteux, et al., Propellants, Explosives, Pyrotechnics **31**, 89 (2006).
10. J. W. Tringe, J. D. Molitoris, L. Smilowitz, et al., AIP Conference Proceedings **1195**, 424 (2009).
11. L. Smilowitz, B. F. Henson, M. M. Sandstrom, et al., Applied Physics Letters **90** (2007).

[12] L. Smilowitz, B. F. Henson, M. M. Sandstrom, et al., in *JANNAF 22nd Propulsion Safety Hazards Subcommittee Meeting* (JANNAF, Charleston, SC, 2005).
[13] T. L. Boggs, Prog Astronaut Aeronaut **90**, 121 (1984).
[14] J. L. Maienschein, J. F. Wardell, M. R. DeHaven, et al., Propellants, Explosives, Pyrotechnics **29**, 287 (2004).
[15] C. B. Skidmore, D. S. Phillips, S. F. Son, et al., AIP Conference Proceedings, 579 (1998).
[16] B. F. Henson, L. Smilowitz, J. J. Romero, et al., AIP Conference Proceedings **955**, 825 (2007).
[17] R. A. Fifer and J. E. Cole, in *Proceedings - 7th Symposium (International) on Detonation.; Annapolis, Md, USA* (Md, USA : US Naval Surface Weapons Cent (NSWC MP 82-334), White Oak, 1982, p. 164.
[18] A. I. Atwood, T. L. Boggs, P. O. Curran, et al., Journal of Propulsion and Power **15**, 740 (1999).
[19] N. Kubota and S. Sakamoto, Propellants Explos Pyrotech **14**, 6 (1989).
[20] L. Glascoe, (unpublished results).
[21] L. Smilowitz, B. F. Henson, J. J. Romero, et al., AIP Conference Proceedings **1195**, 436 (2009).
[22] B. F. Henson, L. Smilowitz, J. J. Romero, et al., AIP Conference Proceedings **1195**, 257 (2009).